JAAS

PAPER

View Article Online
View Journal | View Issue

Cite this: J. Anal. At. Spectrom., 2025, 40, 1733

GHCTWNNM: a gradient histogram constraint truncated WNNM denoising algorithm for LIBS with spectrum-to-image conversion†

Shengjie Ma,[abc] Shilong Xu,*[abc] Congyuan Pan,[d] Jiajie Fang,[abc] Fei Han,[abc] Xi Wang,[a] Yuhao Xia,[abc] Wanying Ding[abc] and Yihua Hu*[abc]

Laser-induced breakdown spectroscopy (LIBS) technology has been widely applied across various fields due to its rapid and straightforward analytical capabilities. However, this technology is susceptible to noise interference during the detection process, which will seriously affect the quantitative analysis accuracy. To mitigate the influence of noise and improve the analysis accuracy, we propose a Gradient Histogram Constraint Truncated Weighted Nuclear Norm Minimization (GHCTWNNM) algorithm for LIBS spectra denoising. Here, we innovatively convert the denoising problem of 1D spectra data into a 2D image denoising problem, where we can take advantage of the superior image denoising technology to enhance the denoising effect of LIBS spectra. On the basis of the traditional WNNM algorithm, we introduce the truncation threshold and gradient histogram constraints, which not only improve the computational efficiency but also prevent distortion issues caused by excessive smoothing of image texture details. Subsequently, we derived the solution of the GHCTWNNM algorithm using the Alternating Direction Method of Multipliers (ADMM) method. The experimental results demonstrate that the GHCTWNNM algorithm achieves a remarkable improvement in denoising performance, with an increase of approximately 6 dB in ΔSNR compared to the WNNM algorithm. Moreover, in comparison with nine other image denoising algorithms, GHCTWNNM not only delivers superior denoising capabilities but also exhibits greater adaptability to different noise environments, especially in a high background noise environment. Additionally, the R^2 of the Al element quantitative analysis result has increased by 0.26 after applying the GHCTWNNM denoising method. In summary, the LIBS denoising method based on the GHCTWNNM algorithm can effectively enhance the spectra SNR and significantly reduce the errors in quantitative analysis caused by noise, thereby enhancing the accuracy and reliability of LIBS. This provides a strong basis for its wide application and further development in various related fields.

Received 12th February 2025
Accepted 6th May 2025

DOI: 10.1039/d5ja00057b

rsc.li/jaas

1. Introduction

In recent years, Laser-induced breakdown spectroscopy (LIBS) has emerged as a prominent technique in the field of elemental analysis. High-energy laser pulses create plasma on the surface of the target, which excites the atoms to emit characteristic spectral lines, enabling the detection of the element composition.[1–3] Celebrated for its user-friendly operation, rapid real-time analysis, non-contact, and simultaneous detection for multiple elements, LIBS has gained widespread application across various fields, including metallurgy,[4–6] environmental monitoring,[7–9] geological surveying,[10,11] biomedicine,[12,13] and so on.

During the interaction of lasers with matter, a series of complex processes such as ablation, excitation, and ionization will take place. This may result in a substantial amount of noise interfering with the spectral acquisition process. In ref. 14, Tognoni *et al.* summarized the noise sources into four categories. The first one is known as source noise, which is caused by fluctuations in the interaction between the laser and the sample or the laser and the plasma. The second is the shot noise, which is due to the number of photons reaching the detector. And the other two are detector noise and instrument (thermal) drift. The interference from these sources of noise can significantly affect the spectra quality as well as the quantitative analysis accuracy. Consequently, denoising in spectral analysis is a critical component of LIBS, playing a significant role in improving spectral quality and quantitative analysis accuracy.

[a]State Key Laboratory of Pulsed Power Laser Technology, National University of Defense Technology, Hefei 230037, People's Republic of China. E-mail: xushi1988@nudt.edu.cn; skl_hyh@163.com

[b]Key Laboratory of Electronic Restriction of Anhui Province, National University of Defense Technology, Hefei 230037, People's Republic of China

[c]Advanced Laser Technology Laboratory of Anhui Province, National University of Defense Technology, Hefei 230037, People's Republic of China

[d]Anhui Province Hefei GStar Intelligent Control Technical Co.Ltd., Hefei, Anhui 230037, China

† Electronic supplementary information (ESI) available. See DOI: https://doi.org/10.1039/d5ja00057b

Methods to improve the Signal-to-Noise Ratio (SNR) of the LIBS spectrum include experimental-based and algorithm-based techniques. The experimental-based technique mainly focuses on optimizing the LIBS experimental parameters, including laser energy,[15] spectrometer delay time,[16] integration time,[17] and so on. For example, we can effectively avoid the interference of continuous background noise by selecting an appropriate value of delay time. The parameters preset in the experimental-based method are usually based on existing experience. In addition, to ensure the best experiment outcomes, these parameters must be further adjusted according to the specific conditions and experiment environment. It is worth noting that while the aforementioned methods of optimizing parameters can significantly reduce the influence of background noise, the spectra acquisition process may still be subjected to noise from other sources. Under these circumstances, it is advisable to consider algorithm-based methods to denoise LIBS spectra. Algorithm-based methods can be categorized into the moving window smoothing algorithms, the power spectrum estimation, and the deep learning-based algorithms.[18] Common moving window smoothing and power spectrum estimation methods include the Savitzky–Golay (SG) filter[19] and Wavelet Transform (WT).[20–22] The WT method is widely used for denoising in various types of data, including LIBS spectra, Raman spectra, near-infrared spectra, and so on. Xie *et al.* proposed an improved WT method and derived the optimal parameters to eliminate noise interference.[20] The results showed that the relative standard deviation values of all trace elements after denoising were reduced, effectively improving the quantitative analysis accuracy in aluminum alloys. Lu *et al.* combined the recursive feature elimination with cross-validation method with WT.[21] This approach overcomes the threshold smoothing issue present in traditional WT methods and can effectively remove noise from the spectra, which can enhance the precision of LIBS quantitative analysis. Additionally, it also facilitates feature selection in the denoised LIBS spectra. Xu *et al.* introduced the entropy analysis theory and proposed two improved threshold analysis theories.[22] The results indicated that when the threshold function was selected as a double exponential function and the modulation transfer function, the quantitative analysis accuracy of Mn, Cr, and Mg elements in aluminum alloys can be significantly improved. However, the robustness and adaptability of WT is poor due to the need for manual parameter selection, and current research is essentially focused on the improvement of the WT method. In addition, the spectra sequences usually have complex characteristics and high dimensions, which makes traditional denoising methods face many challenges.

To address these challenges, the use of deep learning for data denoising has also been researched in recent years. Existing studies predominantly train the deep learning models by the simulated data, and then apply the well-trained models to denoise actual measured signals.[23–25] Although the deep learning-based denoising methods have shown excellent performance, they also require a large amount of data with labels for model training. For LIBS spectra, samples may contain a variety of elements, and there are very rich characteristic spectral lines, which will make it quite complex and challenging to simulate LIBS spectra. Taking the steel slag samples studied in this paper as an example, they contain nine elements such as Fe, Mn, Al, Si, and so on, and the spectral lines of these elements may add up to hundreds. When directly employing the actually measured LIBS spectra for the training of the deep model, issues such as the variable experiment environment, the poor reproducibility of LIBS, and the difficulty in directly measuring the noise will result in inaccurate labels or even make it impossible to assign them directly. Consequently, it is seldom seen that the deep learning method is utilized to directly denoise the LIBS spectra.

In this paper, we introduce a novel approach for spectral denoising. In view of the numerous advanced achievements that have been made in the field of image denoising, we attempt to convert the LIBS signal denoising task into an image-based denoising task. The aim is to take advantage of the inherent strengths of image denoising to enhance the denoising performance. Based on the above analysis, we proposed a Gradient Histogram Constraint Truncated Weighted Nuclear Norm Minimization (GHCTWNNM) denoising algorithm for LIBS with spectrum-to-image conversion. As shown in Fig. 1, the denoising method mainly consists of four steps: sample preparation and spectra acquisition, spectrum dimension conversion, denoising for the 2D LIBS image, and denoising performance evaluation. We firstly propose a new method for converting the spectra sequence into a 2D image, where the characteristic spectral line information of various elements can be effectively preserved. This approach allows for a more comprehensive representation of spectral characteristics in the image. On this basis, for image denoising algorithms, to address the issue of long computation time, as well as to avoid distortion caused by

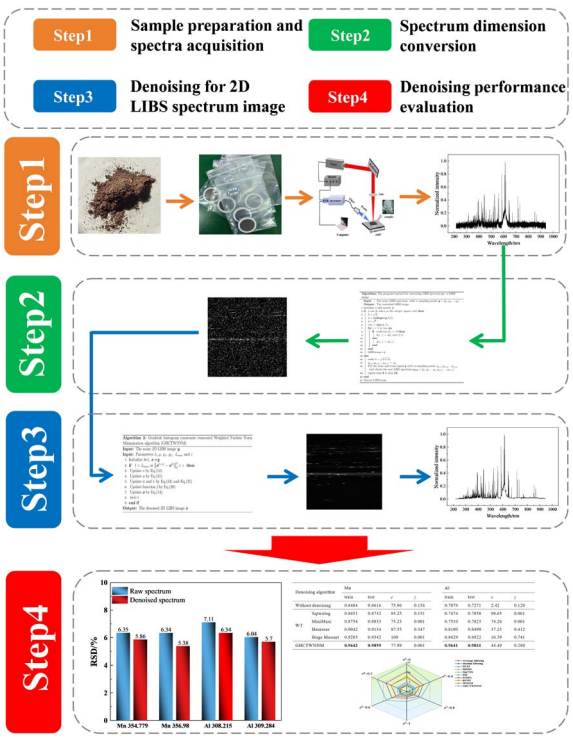

Fig. 1 Flowchart of the LIBS spectrum denoising.

excessive smoothing of image texture details, we introduce the method of truncation points and gradient histogram constraints to improve the WNNM algorithm. Then, we derived the solution of the GHCTWNNM algorithm using the Alternating Direction Method of Multipliers (ADMM) method. To verify the feasibility of our proposed method, we first conducted a comparative analysis of the GHCTWNNM algorithm with nine other image denoising algorithms, and the GHCTWNNM algorithm demonstrates significant advantages, which are reflected in its outstanding performance in LIBS denoising, as well as its greater adaptability to various noise conditions. Subsequently, we also conducted a quantitative analysis of the LIBS spectra before and after denoising. After denoising, the R^2 of the Al element quantitative analysis results increased by approximately 0.26. Additionally, we compared our method with the WT method, and the GHCTWNNM algorithm also demonstrated excellent performance. In summary, the GHCTWNNM algorithm has provided a new denoising idea for LIBS spectra, and it is also expected to be applied in multiple fields such as Raman spectroscopy, near-infrared spectroscopy and so on.

2. Experimental setup and denoising model

2.1 Sample preparation and LIBS spectrum collection

In this paper, we selected 40 steel slag powder samples with different element contents. The sample is shown in Fig. S1(a)† and the concentration of the major components is shown in Table S1.† Considering that the samples are in powder form, which is not conducive to a direct test, we compress the powdered samples into tablets. As shown in Fig. S1(b),† we use the pellet press manufactured by Shanghai Xinnuo Instrument Equipment Co., Ltd, with the model number ZYP-40TS. During the pressing process, we first placed 5 g of the samples and 9 g of boric acid into the mold of the pellet press. Under a pressure of 30 Tons, we pressed for 1 minute. Finally, we can obtain the circular samples with a diameter of approximately 40 mm and a thickness of about 5 mm, as shown in Fig. S1(c).† It is particularly important to note that before preparing each sample, the mold must be cleaned by alcohol to reduce cross-contamination between different samples.

The single-pulse LIBS system used in the experiment is depicted in Fig. 2. The laser beam was reflected and focused vertically onto the sample surface through a lens with a focal length of 75 mm. The prepared samples are mounted on a 3D rotation stage that can spin uniformly to ensure the LIBS spectra data can be collected from different surfaces of the sample. Under the interaction of a high-energy laser with matter, the sample surface is ionized to produce plasma, which is then received by a probe and transmitted to a spectrometer to form the LIBS spectrum. A three-channel Avantes spectrometer is used in our experiment, covering a wavelength range from 216 nm to 942 nm. The positions of the laser source and the probe remain stationary throughout the experiment. Finally, the synchronization between the laser emission and the spectrometer's delay time was maintained with a DG645, and the delay time is set to 2 μs, and the integration time of the spectrometer is set to 1 ms. In this manner, 300 sets of

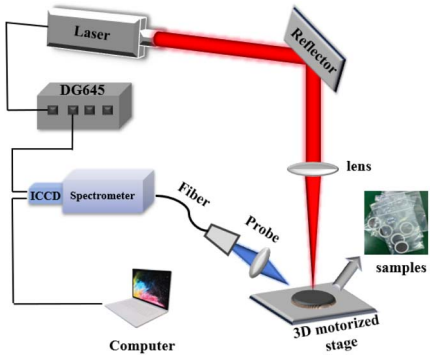

Fig. 2 The schematic diagram of the LIBS experiment.

spectrum data are collected for each sample. Table S2† gives the detailed model and parameters of the experimental instruments.

2.2 Spectrum dimension conversion method

Suppose that the LIBS spectrum signal we obtain is $y = [y_1, y_2, \ldots, y_N]$, where N is the total number of sampling points. Our aim is to convert a $1 \times N$ 1D spectrum signal into an $n \times n$ 2D image, where $n = \sqrt{N}$. In ref. 26, the conversion method adopted by Chen *et al.* is shown in Fig. 3(a). For this method, we only need a simple reshape(y,n,n) command in MATLAB to achieve the conversion from a 1D LIBS spectrum to a 2D image. However, this method also has certain drawbacks. There is a noticeable "jump" between rows of data, as indicated by the red arrow in Fig. 3(a), where the n-th sampling point is at the end of the first row, and the $(n+1)$-th sampling point is at the beginning of the second row. In the 1D spectrum sequence, the two sampling points are continuous, with a distance of one. However, in the 2D image, the distance between them increases to $\sqrt{n^2+1}$ pixels (here, we consider a sampling point as a square, and the distance between two sampling points is defined as the Euclidean distance between the centers of two squares). When performing convolution operations on the 2D image, the

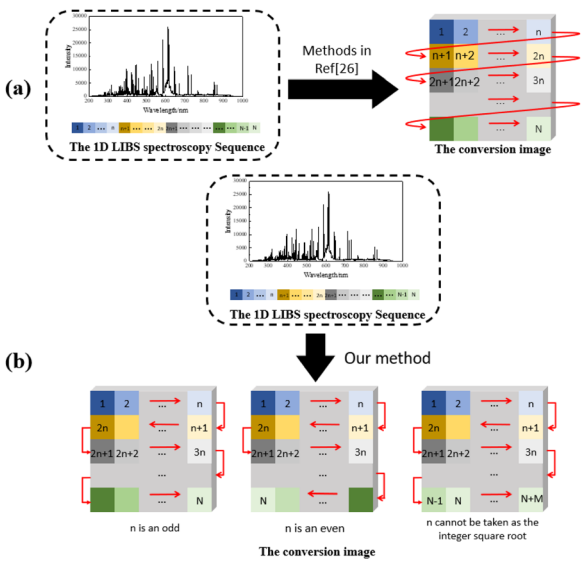

Fig. 3 1D spectrum to 2D image conversion method.

characteristics of the LIBS spectrum may not be effectively extracted and preserved. To address the aforementioned problem, we adopt a more appropriate method for converting the spectrum to images to ensure that the subsequent denoising model can fully extract the features of LIBS images. For the converted 2D image, we aim to keep the distance between adjacent points as small as possible to retain as much prior information as we can. As shown in Fig. 3(b), in our new conversion method, the distance between two adjacent points remains 1 in the 2D image. For example, in Fig. 3(a), there is a clear discontinuity between the points at positions n and $n+1$, $2n$ and $2n+1$, whereas in Fig. 3(b), these points are continuous.

It is worth noting that if N is odd, the position of the N-th point in the 2D image is LIBSimage(n,n). And if N is even, its position is LIBSimage(n,1). For the method shown in Fig. 3(b), we only need to use the flip(.) function to reverse the data in the even rows.

Of course, N may not be square rooted in most cases. For this situation, we need to pad the LIBS spectrum sequence to make $n = \sqrt{N+M}$, where M is the number of padded pixel points. In this paper, the number of sampling points of the spectrometer is $N = 16\,375$, and we can set $M = 9$ to make $n = 128$. As shown in Fig. 3, there are no obvious characteristic peaks at the end of the LIBS spectrum sequence, so we can set the value of the padding pixel points $y_{N+1} - y_{N+M}$ to the value of y_N. We summarize the aforementioned steps in Algorithm 1.

Algorithm 1: The proposed LIBS spectrum dimensional conversion method

Input : The noisy LIBS spectrum with n sampling points $\boldsymbol{y} = [y_1, y_2, ..., y_N]$
Output: The converted LIBS image

Initialize a null matrix $\boldsymbol{z}$;
if *N can be taken as the integer square root* **then**
  $n = \sqrt{N}$;
  $\boldsymbol{z} = \mathbf{reshape}(\boldsymbol{y}, n, n)$;
  $\boldsymbol{z} = \boldsymbol{z}^T$;
  $row = \mathbf{size}(\boldsymbol{z}, 1)$;
  for $i = 1$ *to* row **do**
    if $mod(row, 2) == 0$ **then**
      $\boldsymbol{z}(i, :) = \boldsymbol{z}$(i, end:-1:1);
    else
      $\boldsymbol{z}(i, :) = \boldsymbol{z}(i,:)$;
    end
  end
  LIBS$image$=$\boldsymbol{z}$;
else
  make $n = \sqrt{N+M}$;
  $y_{N+1}, y_{N+2}, ..., y_{N+M} \leftarrow y_N$;
  Fill the noise spectrum signal $\boldsymbol{y}$ with m sampling points $y_{N+1}, y_{N+2}, ..., y_{N+M}$ and obtain the new LIBS spectrum $\mathbf{y_{Fill}} = [y_1, y_2, ..., y_N, y_{N+1}, ..., y_{N+M}]$;
  repeat step **4** to step **14**;
end
Return LIBS$image$

By using this new method, we can convert the 1D LIBS spectrum signal into a 2D grayscale image with the size of $n \times n$. Then we can transform the 1D spectra signal denoising problem to 2D image processing. Ultimately, we can apply various image denoising techniques to enhance the noise reduction performance.

Taking sample no. 1 as an example, the 2D LIBS images obtained by different methods are shown in Fig. 4. We also employed the Gramian Angular Field (GAF) method[27] to convert the 1D LIBS spectrum into 2D images. The GAF can be divided into the Gramian Angular Summation/Difference Field (GASF/GADF). The conversion principle can be found in the supplementary. It is worth noting that the size of the 2D LIBS images obtained using the GASF and GADF method is $N \times N$. Finally, to better evaluate the denoising performance of different

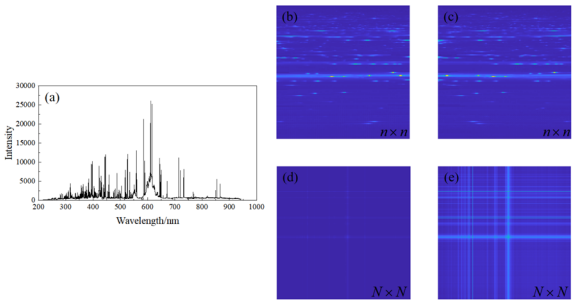

Fig. 4 The 2D LIBS images of sample no. 1 obtained by different methods. (a) The raw LIBS spectrum, and (b)–(e) the 2D LIBS images obtained using the methods in Fig. 3(a) and (b), GASF, and GADF, respectively. (The images we used for denoising are grayscale images, and to better observe the image details, we are displaying non-grayscale images here. The grayscale images can be found in Fig. S2.†).

methods, we conducted the quantitative analysis of the LIBS spectrum, where the inverse conversion is involved here, and the 2D image needs to be restored to a 1D spectra signal. We simply need to perform steps 7–13 in Algorithm 1 and then flatten the LIBS image matrix. For the GAF method, we have also described the inverse conversion process in the ESI.†

2.3 The GHCTWNNM denoising algorithm

The purpose for denoising the 2D LIBS image is to separate the clean image $\boldsymbol{X}$ from the noisy image $\boldsymbol{Y}$. The solution model can be represented as:

$$\boldsymbol{Y} = \boldsymbol{X} + \boldsymbol{N} \tag{1}$$

where $\boldsymbol{N}$ is the noise, the size of $\boldsymbol{Y}$ is $n \times n$, and $n = 128$. The noise in LIBS spectra is typically the Gaussian noise with zero-mean and a variance of ${\sigma_n}^2$.[22] Therefore, the denoised image can be solved using the following optimization objective

$$\hat{\boldsymbol{X}} = \arg\min_{\boldsymbol{X}} \frac{1}{2{\sigma_n}^2} \|\boldsymbol{Y} - \boldsymbol{X}\|_F^2 + \lambda \mathrm{rank}(\boldsymbol{X}) \tag{2}$$

where $\|\cdot\|_F^2$ is the Frobenius norm, rank$(\cdot)$ is the rank of the matrix, and λ is the trade-off parameter. However, since the rank minimization problem is non-convex, the solution of eqn (2) is NP-hard. The Nuclear Norm Minimization (NNM) can be used to transform the solution of eqn (2) into a convex optimization problem in eqn (3).

$$\hat{\boldsymbol{X}} = \arg\min_{\boldsymbol{X}} \frac{1}{2{\sigma_n}^2} \|\boldsymbol{Y} - \boldsymbol{X}\|_F^2 + \lambda \|\boldsymbol{X}\|_* \tag{3}$$

where $\|\boldsymbol{X}\|_* = \sum_j \sigma_i(\boldsymbol{X})$ is the nuclear norm and $\sigma_i(\boldsymbol{X})$ is the i-th singular value of $\boldsymbol{X}$. Generally speaking, larger singular values represent greater energy, while the smaller singular values represent noise. In the NNM algorithm, we assign the same weight to all singular values. But in practice, we hope to retain more singular values with larger numerical values and filter out those with small numerical values. In this way, we can better preserve the main information in the image. The Weighted Nuclear Norm Minimization (WNNM) method[28] can address the

aforementioned issue by assigning different weights to different singular values, and the optimization objective of WNMM is

$$\hat{\boldsymbol{X}} = \arg\min_{\boldsymbol{X}} \frac{1}{2\sigma_n^2}\|\boldsymbol{Y}-\boldsymbol{X}\|_F^2 + \lambda\|\boldsymbol{X}\|_{w,*} \tag{4}$$

where $\|\boldsymbol{X}\|_{w,*} = \sum_i w_i\sigma_i(\boldsymbol{X})$ is the weighted nuclear norm of $\boldsymbol{X}$ and w_i represents the weights for different singular values.

$$w_i = \frac{c\sqrt{N}}{\sigma_i(\boldsymbol{X})+\varepsilon} \tag{5}$$

where ε is very small to avoid dividing by zero and c is a positive constant. In eqn (5), the weight is inversely proportional to the size of the singular value, which allows for assigning smaller weights to larger singular values. This method helps to better preserve the main information. Assuming the weights satisfy $0 \le w_1 \le w_2 \le$,…, $\le w_n$, then the solution of eqn (4) can be expressed as

$$\hat{\boldsymbol{X}} = \boldsymbol{U}\boldsymbol{S}_W(\Sigma)\boldsymbol{V}^T \tag{6}$$

where $\boldsymbol{Y} = \boldsymbol{U}\boldsymbol{\Sigma}\boldsymbol{V}^T$ is the Singular Value Decomposition (SVD) of $\boldsymbol{Y}$, and $\boldsymbol{S}_W(\Sigma) = \max(\Sigma_{ii} - w_i, 0)$ is the soft thresholding operator. In the actual solution process, we can employ the non-local self-similarity (NSS) method. The principle of the NSS method is that there often exist many similar small patches in the image, which may be far apart but have a high degree of similarity, and this characteristic is known as the self-similarity of images. For a noise-free and clean image $\boldsymbol{X}$, we can divide it into k patches $\{\boldsymbol{x}_i\}_{i=1}^{k}$. However, it is difficult to obtain $\boldsymbol{X}$ for actual measured signals even in this way. Therefore, we can choose to construct a noisy image $\boldsymbol{Y}$ and divide it into corresponding patches $\{\boldsymbol{y}_i\}_{i=1}^{k}$. And then, the problem of restoring a clean image $\boldsymbol{X}$ from a noisy image $\boldsymbol{Y}$ can be transformed into obtaining $\boldsymbol{x}_i$ from $\boldsymbol{y}_i$. And the ultimate optimization goal can be expressed as:

$$\hat{\boldsymbol{x}} = \arg\min_{\boldsymbol{x}} \frac{1}{2}\|\boldsymbol{y}-\boldsymbol{x}\|_2^2 + \mu\|\boldsymbol{x}\|_{w,*} \tag{7}$$

Although the WNNM algorithm addresses the issue of singular value weighting, there are still two problems. The first one is that the WNMM algorithm performs an SVD decomposition on y during each iteration, which is a time-consuming process. And the second one is that the WNNM algorithm may cause image texture details to be distorted due to excessive smoothing, which will reduce the visual quality of the image. In response to the aforementioned two issues, we propose the GHCTWNNM algorithm. The GHCTWNNM algorithm primarily aims to improve the two main problems mentioned.

For the first problem, as previously stated, smaller singular values correspond to noise. Therefore, a truncation method can be used to remove the smaller singular values. Here we define $\|\boldsymbol{x}\|_{Tw,*} = \sum_{i=1}^{T-1}\sigma_i(\boldsymbol{x}) + \sum_{i=T}^{n} w_i\sigma_i(\boldsymbol{x})$ as the truncated weighted nuclear norm, where T is the truncation point. From the definition of the truncated weighted nuclear norm, we can perform soft thresholding starting from the $T+1$-th singular value, and the first T singular values remain unchanged. Therefore, the optimization objective of the truncated WNNM method can be rewritten as:

$$\hat{\boldsymbol{x}} = \arg\min_{\boldsymbol{x}} \frac{1}{2}\|\boldsymbol{y}-\boldsymbol{x}\|_2^2 + \mu\|\boldsymbol{x}\|_{Tw,*} \tag{8}$$

For the second problem, we employ a gradient histogram matching prior model to preserve the texture details in the image. Generally, the closer the gradients of the denoised image are to those of the original image, the better the denoising performance tends to be. Therefore, we first need to find the gradient histogram $\boldsymbol{h}_r$ of the original image to obtain the matching prior. Our goal is to make the gradient histogram of the denoised image $\boldsymbol{h}_f$ as close as possible to $\boldsymbol{h}_r$. Finally, after introducing the regularization term $R(\boldsymbol{x})$ and adding the gradient histogram constraint, eqn (8) can be rewritten as:

$$\arg\min_{\boldsymbol{x}}\left\{\frac{1}{2}\|\boldsymbol{y}-\boldsymbol{x}\|_2^2 + \mu\|\boldsymbol{x}\|_{Tw,*} + \gamma R(\boldsymbol{x})\right\} \quad \text{s.t. } \boldsymbol{h}_f = \boldsymbol{h}_r \tag{9}$$

where $R(\boldsymbol{x}) = \|\nabla\boldsymbol{x}\|_2^2 + \beta\|f(\nabla\boldsymbol{x}) - \nabla\boldsymbol{x}\|_2^2$ is the regularization term, γ and β are the regularization parameters, $\nabla\boldsymbol{x}$ is the gradient of $\boldsymbol{x}$, and $f(\cdot)$ is a monotonically non-decreasing odd function in $(0,+\infty)$. To solve eqn (9), we also need to calculate the gradient histogram $\boldsymbol{h}_r$ of the original image. For this purpose, we adopt the method described in ref. 29. Zuo *et al.* transformed the estimation problem of $\boldsymbol{h}_r$ into a deconvolution problem.

$$\boldsymbol{h}_r = \underset{\boldsymbol{h}_x}{\operatorname{argmin}}\|\boldsymbol{h}_y - \boldsymbol{h}_x \otimes \boldsymbol{h}_g\|_2^2 + cR(\boldsymbol{h}_x) \tag{10}$$

where $R(\boldsymbol{h}_x)$ is the regularization term based on the prior information of LIBS image gradient histograms, c is a constant, and $\otimes$ is the convolution operator.

Subsequently, we can solve eqn (9) in conjunction with eqn (10). We first introduce two parameters u and v, where u and v have the same dimensions as $\boldsymbol{h}_f$ and $R(\boldsymbol{x})$. And eqn (9) can be rewritten as

$$\begin{aligned}&\arg\min_{\boldsymbol{x},u,v}\left\{\frac{1}{2}\|\boldsymbol{y}-\boldsymbol{x}\|_2^2 + \mu\|\boldsymbol{x}\|_{Tw,*} + \gamma u\right\}\\ &\text{s.t. } u = R(\boldsymbol{x}) \quad v = \boldsymbol{h}_f \quad v = \boldsymbol{h}_r\end{aligned} \tag{11}$$

The corresponding augmented Lagrangian function of eqn (11) can be expressed as

$$\begin{aligned}L(\boldsymbol{x},u,v,\hat{u},\hat{v}) = {}& \frac{1}{2}\|\boldsymbol{y}-\boldsymbol{x}\|_2^2 + \mu\|\boldsymbol{x}\|_{Tw,*} + \gamma u\\ &+ \frac{\rho_1}{2}\|u - R(\boldsymbol{x}) + \hat{u}\|_2^2 + \frac{\rho_2}{2}\|v - \boldsymbol{h}_f + \hat{v}\|_2^2\end{aligned} \tag{12}$$

Then, the solution of eqn (9) can be expressed as

$$\arg\min_{\boldsymbol{x},u,v} L(\boldsymbol{x},u,v,\hat{u},\hat{v}) = \arg\min_{\boldsymbol{x},u,v}\left\{\begin{aligned}&\frac{1}{2}\|\boldsymbol{y}-\boldsymbol{x}\|_2^2\mu\|\boldsymbol{x}\|_{Tw,*} + \gamma u\\ &+\frac{\rho_1}{2}\|u - R(\boldsymbol{x}) + \hat{u}\|_2^2 + \frac{\rho_2}{2}\|v - \boldsymbol{h}_f + \hat{v}\|_2^2\end{aligned}\right\} \quad \text{s.t. } v = \boldsymbol{h}_r \tag{13}$$

where ρ_1 and ρ_2 are two penalty parameters. It is clear that solving eqn (13) directly is very difficult. Here, we can adopt the Alternating Direction Multiplier Method (ADMM)[30–32] method. The ADMM method is used to solve decomposable convex optimization problems, and it breaks down the original complex optimization problem into several solvable sub-problems, and solves each sub-problem in parallel. Finally, the solutions of these sub-problems are coordinated to obtain a global solution for the original problem. At the l-th iteration, we can transform the solution of eqn (13) into the following five sub-problems.

(a) Updating $\boldsymbol{x}$. To update $\boldsymbol{x}$, we should solve the following optimization problem

$$\begin{aligned}\boldsymbol{x}^{(l+1)} &= \underset{\boldsymbol{x}^{(l)}}{\operatorname{argmin}}\, L\left(\boldsymbol{x}^{(l)}, u^{(l)}, v^{(l)}, \hat{u}^{(l)}, \hat{v}^{(l)}\right) \\ &= \underset{\boldsymbol{x}^{(l)}}{\operatorname{argmin}} \left\{ \begin{array}{l} \frac{1}{2}\|\boldsymbol{y} - \boldsymbol{x}^{(l)}\|_2^2 + \mu\|\boldsymbol{x}^{(l)}\|_{Tw,*} \\ +\frac{\rho_1}{2}\|u - R\left(\boldsymbol{x}^{(l)}\right) + \hat{u}\|_2^2 \end{array} \right\} \end{aligned} \tag{14}$$

We can employ the gradient descent method combined with soft thresholding operations to solve eqn (14). It should be noted that in the process of calculating the gradient of $L(\boldsymbol{x},u,v,\hat{u},\hat{v})$, the truncated nuclear norm term $\mu\|\boldsymbol{x}^{(l)}\|_{Tw,*}$ is the non-smooth part to x, and its gradient requires special treatment. Here, we use the soft thresholding operation to handle its update. We define $\boldsymbol{Q} = \frac{1}{2}\|\boldsymbol{y} - \boldsymbol{x}^{(l)}\|_2^2 + \frac{\rho_1}{2}\|u - R(\boldsymbol{x}^{(l)}) + \hat{u}\|_2^2$, and its gradient can be calculated as follows

$$\nabla_x \boldsymbol{Q}\left(\boldsymbol{x}^{(l)}\right) = -\left(\boldsymbol{y} - \boldsymbol{x}^{(l)}\right) + \rho_1\left(u^{(l)} - R\left(\boldsymbol{x}^{(l)}\right) + \hat{u}^{(l)}\right)\nabla_x R\left(\boldsymbol{x}^{(l)}\right) \tag{15}$$

Since the truncated nuclear norm is not differentiable at points where the singular values are zero, here we need to compute the sub-gradient of $\mu\|\boldsymbol{x}^{(l)}\|_{Tw,*}$. The sub-gradient of the nuclear norm is the sign of the corresponding singular values, and it can be expressed as

$$\frac{\partial \mu\|\boldsymbol{x}^{(l)}\|_{Tw,*}}{\partial \boldsymbol{x}} = \mu\begin{bmatrix} \operatorname{sign}\left(\sigma_1\left(\boldsymbol{x}^{(l)}\right)\right), \operatorname{sign}\left(\sigma_2\left(\boldsymbol{x}^{(l)}\right)\right), \ldots, \\ \operatorname{sign}\left(\sigma_{T-1}\left(\boldsymbol{x}^{(l)}\right)\right), w_T \operatorname{sign}\left(\sigma_T\left(\boldsymbol{x}^{(l)}\right)\right), \\ w_{T+1}\operatorname{sign}\left(\sigma_{T+1}\left(\boldsymbol{x}^{(l)}\right)\right), \ldots, w_n \operatorname{sign}\left(\sigma_n\left(\boldsymbol{x}^{(l)}\right)\right) \end{bmatrix}^T \tag{16}$$

Then, we use the gradient descent method to update $\boldsymbol{x}^{(l)}$

$$\boldsymbol{g}^{(l)} = \boldsymbol{x}^{(l)} - \alpha\left(\begin{array}{l} -\left(\boldsymbol{y} - \boldsymbol{x}^{(l)}\right) + \rho_1\left(u^{(l)} - R\left(\boldsymbol{x}^{(l)}\right) + \hat{u}^{(l)}\right)\nabla_x R\left(\boldsymbol{x}^{(l)}\right) \\ +\mu\begin{bmatrix} \operatorname{sign}\left(\sigma_1\left(\boldsymbol{x}^{(l)}\right)\right), \operatorname{sign}\left(\sigma_2\left(\boldsymbol{x}^{(l)}\right)\right), \ldots, \\ \operatorname{sign}\left(\sigma_{T-1}\left(\boldsymbol{x}^{(l)}\right)\right), w_T \operatorname{sign}\left(\sigma_T\left(\boldsymbol{x}^{(l)}\right)\right), \\ w_{T+1}\operatorname{sign}\left(\sigma_{T+1}\left(\boldsymbol{x}^{(l)}\right)\right), \ldots, w_n \operatorname{sign}\left(\sigma_n\left(\boldsymbol{x}^{(l)}\right)\right) \end{bmatrix}^T \end{array}\right) \tag{17}$$

where α is the learning rate and $\boldsymbol{g}^{(l)}$ is the intermediate variable. Subsequently, we perform SVD on $\boldsymbol{g}^{(l)}$ and obtain $\boldsymbol{g}^{(l)} = U\Sigma V^T$. We define the soft thresholding term as $\operatorname{soft}_{tw_i}(\sigma_i(\boldsymbol{g}^{(l)}))$ and apply soft thresholding to the singular values, where tw_i is the thresholding term, and t is a constant. The method of determining the value of w_i is consistent with the method used in the truncated nuclear norm. Then we define

$$\Sigma' = \operatorname{diag}\begin{bmatrix} \operatorname{soft}_t(\sigma_1), \operatorname{soft}_t(\sigma_2), \ldots, \operatorname{soft}_t(\sigma_{T-1}), \\ \operatorname{soft}_{tw_T}(w_T\sigma_T), \operatorname{soft}_{tw_{T+1}}(w_{T+1}\sigma_{T+1}), \\ \ldots, \operatorname{soft}_{tw_n}(w_n\sigma_n) \end{bmatrix} \tag{18}$$

Finally, we can reconstruct $\boldsymbol{x}^{(l+1)}$ as

$$\boldsymbol{x}^{(l+1)} = U\Sigma' V^T \tag{19}$$

(b) Updating v. Given a fixed $\boldsymbol{x}$, the v sub-problem becomes

$$\begin{aligned} v^{(l+1)} &= \underset{v^{(l)}}{\operatorname{argmin}}\, L\left(\boldsymbol{x}^{(l+1)}, u^{(l)}, v^{(l)}, \hat{u}^{(l)}, \hat{v}^{(l)}\right) \\ &= \underset{v^{(l)}}{\operatorname{argmin}}\left\{\frac{\rho_2}{2}\|v^{(l)} - \boldsymbol{h}_f + \hat{v}^{(l)}\|_2^2\right\} \\ &\text{s.t. } v = \boldsymbol{h}_r \end{aligned} \tag{20}$$

For eqn (20), under the constraint of $v = \boldsymbol{h}_r$, we can have $v^{(l+1)} = \boldsymbol{h}_r$.

(c) Updating u. If we have a fixed $\boldsymbol{x}$ and v, the u sub-problem becomes

$$\begin{aligned} u^{(l+1)} &= \underset{u^{(l)}}{\operatorname{argmin}}\, L\left(\boldsymbol{x}^{(l+1)}, u^{(l)}, v^{(l+1)}, \hat{u}^{(l)}, \hat{v}^{(l)}\right) \\ &= \underset{u^{(l)}}{\operatorname{argmin}}\left\{\gamma u^{(l)} + \frac{\rho_1}{2}\|u^{(l)} - R\left(\boldsymbol{x}^{(l)}\right) + \hat{u}^{(l)}\|_2^2\right\} \end{aligned} \tag{21}$$

This is a standard quadratic programming problem, where the objective function is a summation of a linear term and a quadratic term to u. Here, we can solve it using an analytical solution method. The derivative of eqn (21) with u is

$$\frac{\partial}{\partial u}\left(\gamma u + \frac{\rho_1}{2}\|u - R\left(\boldsymbol{x}^{(l)}\right) + \hat{u}\|_2^2\right) = \gamma + \rho_1\left(u - R\left(\boldsymbol{x}^{(l)}\right) + \hat{u}\right) \tag{22}$$

Setting eqn (21) to zero and we can have

$$u^{(l+1)} = R\left(\boldsymbol{x}^{(l+1)}\right) - \hat{u}^{(l)} - \frac{\gamma}{\rho_1} \tag{23}$$

(d) Updating the dual variable. The update equations for the dual variable are

$$\hat{u}^{(l+1)} = \hat{u}^{(l)} + u^{(l+1)} - \boldsymbol{h}_f \tag{24}$$

$$\hat{v}^{(l+1)} = \hat{v}^{(l)} + v^{(l+1)} - R(\boldsymbol{x}^{(l+1)}) \tag{25}$$

(e) Updating function f. Once $\boldsymbol{x}$ is fixed, we can determine the function f by solving eqn (26).

$$\underset{f}{\operatorname{argmin}} \|f(\nabla \boldsymbol{x}) - \nabla \boldsymbol{x}\|_2^2 \quad \text{s.t. } \boldsymbol{h}_f = \boldsymbol{h}_r \tag{26}$$

We can solve eqn (26) using the standard histogram normalization operators method[33] to make $\boldsymbol{h}_f$ close to $\boldsymbol{h}_r$.

Combining the above analysis, we summarize the proposed GHCTWNNM algorithm in Algorithm 2. Here, we set the condition for terminating the algorithm iterations to $\|\boldsymbol{x}^{(l+1)} - \boldsymbol{x}^{(l)}\|_2^2 < \varepsilon$.

Algorithm 2: Gradient histogram constraint truncated Weighted Nuclear Norm Minimization algorithm (GHCTWNNM)

Input: The noisy 2D LIBS image $\boldsymbol{y}$
Input: Parameters λ, μ, ρ_1, ρ_2, L_{max} and ε
1: Initialize $l=1$, $\boldsymbol{x}=\boldsymbol{y}$
2: **if** $l < L_{max}$ or $\|\boldsymbol{x}^{(l+1)} - \boldsymbol{x}^{(l)}\|_2^2 < \varepsilon$ **then**
3: Update v by Eq.(12)
4: Update u by Eq.(21)
5: Update $\hat{u}$ and $\hat{v}$ by Eq.(24) and Eq.(25)
6: Update function f by Eq.(26)
7: Update $\boldsymbol{x}$ by Eq.(14)
8: $l=l+1$
9: **end if**
Output: The denoised 2D LIBS image $\boldsymbol{x}$

2.4 Performance evaluation

In this paper, the method we adopt is to convert the 1D LIBS spectrum into a 2D image for denoising. ΔSNR is adopted as the denoising performance evaluation, where $\Delta\text{SNR} = \text{SNR}_{\text{denoised}} - \text{SNR}_{\text{original}}$ is the difference in SNR at the element characteristic spectral line between the denoised and the original spectra. A higher value of ΔSNR indicates more SNR improvement at these characteristic spectral lines, demonstrating superior noise suppression capability. Assuming the peak spectrum intensity of the characteristic spectral line is I, I_{baseline} is the intensity of the baseline, and ${\sigma_{\text{noise}}}^2$ is the noise variance. Then we can define the SNR of the characteristic spectral line as

$$\text{SNR} = \frac{I - I_{\text{baseline}}}{{\sigma_{\text{noise}}}^2} \tag{27}$$

Additionally, to more comprehensively analyze the denoising performance, we also carried out the quantitative analysis and spectra stability analysis on the LIBS spectra before and after denoising. The Partial Least Squares Regression (PLSR) and Support Vector Regression (SVR) methods are the two most common methods for quantitative analysis.[34–37] In this paper, we combine the Particle Swarm Optimization (PSO) algorithm with SVR for multivariate analysis, where the PSO algorithm is used to solve for two parameters in SVR: the penalty factor c and the radial basis kernel function γ. The Correlation Coefficient (R^2) is often used to evaluate the accuracy of the quantitative analysis model. And the Relative Standard Deviation (RSD) can be used to evaluate the spectral stability. The smaller the RSD, the higher the LIBS stability.

$$R^2 = 1 - \frac{\sum_{i=1}^{N}\left(C_i - C_i'\right)^2}{\sum_{i=1}^{N}\left(C_i - \overline{C}_i\right)^2} \tag{28}$$

$$\text{RSD}\ (\%) = \frac{S}{\overline{C}} \times 100\% = \frac{\sqrt{\sum_{i=1}^{M}\left(C_i - \overline{C}\right)^2}}{\overline{C}} \times 100\% \tag{29}$$

where C_i is the actual value of concentration, C_i' is the predicted value, and $\bar{C}$ is the mean of C_i. N is the number of samples, S is the standard deviation, and $L = 300$ is the number of measurements.

3. Results and discussion

3.1 The influence of laser energy on spectrum noise

Firstly, we analyze the effect of experimental-based methods on LIBS spectra SNR. Here, we take the laser energy as an example, and in order to ensure the integrity of steel slag samples and prevent any potential impact on subsequent experimental outcomes, we choose the aluminum sheets as samples. Fig. 5(a)–(d) show the LIBS spectrum collected from the aluminum sheet under different laser energies. When the laser energy is 10 mJ, the LIBS spectrum shown in Fig. 5(d) is essentially all continuous background interference, with the characteristic spectral lines of the Al element being completely submerged in the noise. As the laser energy gradually increases, the peak intensity of the Al element characteristic spectral lines also gradually increases, and there is an obvious improvement in the background noise.

Take the characteristic spectral line at Al: 396.14 nm as an example, we have fitted the baselines of the spectra in

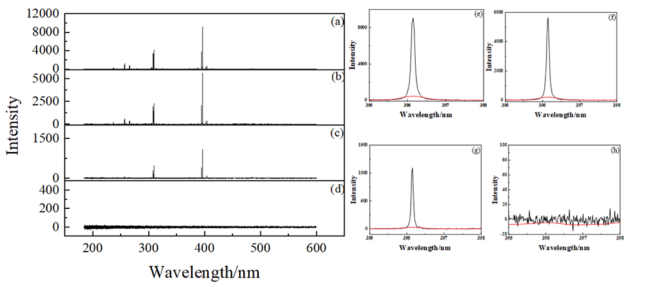

Fig. 5 The LIBS spectrum collected under different laser energies. (a)–(d) The laser energies are 100 mJ, 70 mJ, 40 mJ, and 10 mJ, respectively. (e)–(h) are the characteristic spectral lines at Al: 396.14 nm.

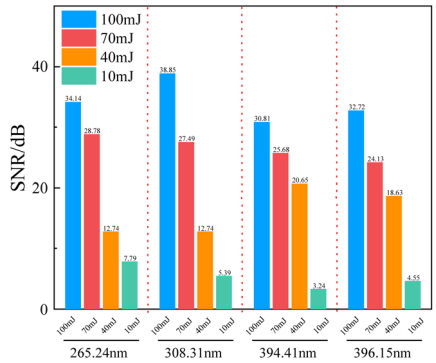

Fig. 6 SNR of four characteristic spectral lines of the Al element with different laser energies.

Fig. 5(a)–(d) and marked them with red lines in Fig. 5(e)–(h). Here the Asymmetric Penalty Least Squares (AsPLS) method[38] is employed to fit the baseline. The parameters are set as follows: an asymmetric factor of 10^{-5}, a threshold of 0.05, a smoothing factor of 4, and a total of 50 iterations. Based on the aforementioned definition, we calculated the SNR of four characteristic spectral lines of the Al element with different laser energies, and the results are shown in Fig. 6. According to the results in Fig. 6, we can observe that with the increase of laser energy, the SNR of all the four characteristic spectral lines has significantly improved. It should be noted here that while increasing the laser energy, the intensity of the background noise will also increase. As shown in Fig. 5(e) and (f), when the laser energy is increased from 70 mJ to 100 mJ, the intensity of the background noise at the spectral line of Al: 396.14 nm increases from 207.91 to 444.2. Nevertheless, increasing the laser energy will enhance the SNR, and this is because the enhancement of laser energy on the signal is greater than that on the noise.[39]

Based on the conclusions in Fig. 5 and 6, we can significantly enhance the spectrum SNR and reduce the interference of background noise by increasing the laser energy. However, the LIBS spectra we collect may still be subject to noise interference from other sources. In such cases, it is essential to directly analyze the spectrum itself in order to achieve effective noise reduction. In the subsequent section, we will apply the proposed GHCTWNNM algorithm to denoise LIBS spectra.

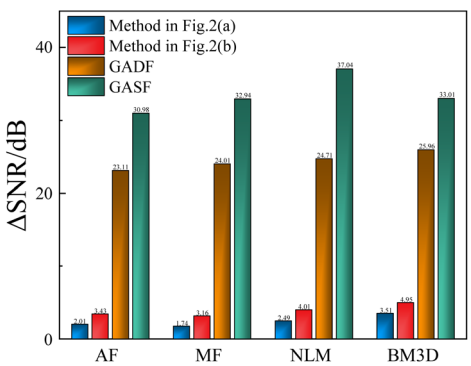

Fig. 7 Comparison of denoising performance for four spectrum dimension conversion methods.

3.2 Denoising Performance of the GHCTWNNM algorithm

3.2.1 Comparison of spectrum dimension conversion methods. We compared the performance of four conversion methods from the 1D LIBS spectrum into 2D image. Here, we used the four most common image denoising methods, the Average Filtering (AF), the Median Filtering (MF), the Non-Local Means (NLM), and the Block-Matching and 3D Filtering (BM3D). Here, we also take the characteristic spectral line at Al: 396.14 nm as an example, and the denoising results are shown in Fig. 7(a) and (b). According to Fig. 7, we can find that our proposed method for converting 1D LIBS spectra to 2D images has achieved an approximately 1.5 dB improvement in ΔSNR compared to the method in ref.26. This indicates that the images obtained by our proposed method can better adapt to existing image denoising algorithms, which will further improve the denoising performance. In addition, we also compared our method with GADF and GASF. Among the four conversion methods, the GASF method performed the best. The reason is that the generated GASF images map the spectrum information into a polar coordinate system, preserving all the structure information of the original spectrum. However, it is worth noting that the dimensions of the 2D LIBS spectrum image obtained by GADF and GASF are both 16 375 × 16 375, which leads to a significant increase in computational cost. When applying a 3 × 3 kernel mean filtering method to the images obtained from GADF and GASF, the required number of computations is $16\,373 \times 16\,373 \times 9 + 4 \times 4 + 16\,373 \times 4 \times 6 = 2.4131 \times 10^9$ additions and $16\,373 \times 16\,373 = 268\,075\,129$ divisions. In contrast, our proposed conversion method requires only $126 \times 126 \times 9 + 4 \times 4 + 126 \times 4 \times 6 = 145\,924$ additions and $128 \times 128 = 16\,384$ divisions. In contrast, both addition and division are reduced by more than 16 000 times. Table 1 provides the time consumption for denoising the

Table 1 Time consumption of different denoising methods

	1D to 2D methods			
Time consumed/s	Method in Fig. 2(a)	Method in Fig. 2(b)	GADF	GASF
AF	1.42	1.38	422.08	437.64
MF	1.43	1.40	217.21	217.52
NLM	1.32	1.38	934.35	955.24
BM3D	1.42	1.41	994.85	965.34

obtained 2D LIBS images using four image denoising algorithms. Although the GASF method has the best denoising performance, the time consumption also increases by nearly 400 times. Furthermore, the time consumption in Table 1 is only for one single image. As the number of samples increases, the time required by this method will also grow, and in some cases, the excessive computational load may even make model training difficult.

3.2.2 2D LIBS image denoising performance analysis. We utilize the spectrum dimension conversion method proposed in section 2.2 to obtain 2D LIBS images, and then apply the GHCTWNNM algorithm presented in section 2.3 for image denoising. We first analyzed the impact of the truncation point T on the GHCTWNNM algorithm performance. Taking the sample no. 1 as an example, Fig. 8 shows the effect of the truncation parameter T on the denoising performance. As the value of T increases, the performance of the algorithm also gradually increases. Additionally, we found that when $T > 5$, with further increases in T, the improvement of the GHCTWNNM algorithm is not very significant, and the ΔSNR gradually converges. When T increases from 5 to 12, the value of ΔSNR only increases by 0.1. At the same time, as T increases, fewer singular values in the truncated weighted nuclear norm are weighted, and the algorithm gradually degenerates into NNM. Therefore, we set the value of T to 5.

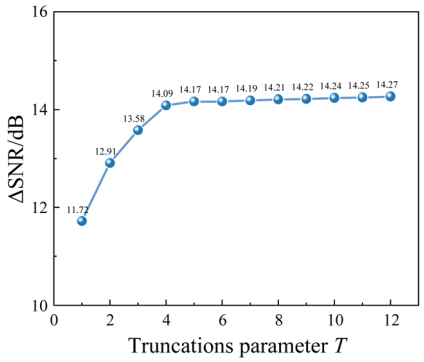

Fig. 8 The influence of the truncation parameter T on the GHCTWNNM algorithm.

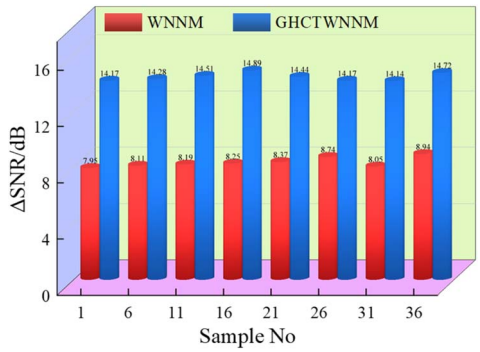

Fig. 9 Denoising performance of GHCTWNNM and WNNM algorithms.

Subsequently, we selected samples no. 1, 6, 11, 16, 21, 26, 31, and 36 to generate the corresponding 2D LIBS images, and compared the denoising performance with WNNM. The ΔSNR results of the two algorithms are shown in Fig. 9. Compared to the WNNM algorithm, the GHCTWNNM algorithm shows an approximate 6 dB improvement in ΔSNR for the denoising results. This is mainly related to the two-point optimization of the algorithm, which significantly improves the denoising performance, especially in the aspect of preserving image details and edge information.

Furthermore, we compared the denoising performance of the GHCTWNNM algorithm with other algorithms; the ΔSNR results are shown in Table 2. The results indicate that our proposed GHCTWNNM algorithm consistently outperforms other algorithms across all samples, with an average ΔSNR of 14.42 dB. Additionally, the Self-Organizing Map Algorithm (SOMA) also achieves relatively satisfactory denoising performance, with an average ΔSNR of 10.57 dB. However, the performance of some traditional denoising methods is not satisfactory, such as mean filtering and median filtering. It is worth noting that the DnCNN model in Table 2 is derived from ref. 40. Zhang *et al.* trained the DnCNN model (**https://github.com/cszn/DnCNN**) using the Berkeley Segmentation Dataset (BSD68), and we directly applied the pre-trained model for LIBS image denoising. However, the experimental results demonstrate that the training effect of the DnCNN model is far from satisfactory. A possible reason may be the differences in the data used to train the model, which also

Table 2 The ΔSNR of different denoising algorithms

	Denoising algorithm									
Sample no	AF	MF	NLM	BM3D	DnCNN	PM	SOMA	kSVD	WNNM	GHCTWNNM
1	3.43	3.16	4.01	4.95	3	4.06	10.35	7.28	7.95	**14.17**
6	3.57	3.41	4.11	5.11	3.01	4.11	10.26	7.27	8.11	**14.28**
11	3.69	4.09	4.26	5.26	3.16	4.26	10.37	7.74	8.19	**14.51**
16	3.4	3.82	3.91	5.9	3.3	3.91	10.74	7.64	8.25	**14.89**
21	3.69	4.02	4.49	5.65	3.11	4.64	10.85	7.33	8.37	**14.44**
26	3.98	4.05	4.45	5.44	2.87	4.44	10.46	8.02	8.74	**14.17**
31	4.24	4.4	4.42	5.42	3.31	4.41	10.91	7.51	8.05	**14.14**
36	3.63	4.01	4.56	5.55	3.51	4.56	10.62	7.23	8.94	**14.72**
Avg.	3.70	3.87	4.27	5.41	3.16	4.30	10.57	7.50	8.33	**14.42**

Table 3 Time and space complexity of different algorithms

Denoising algorithm	Algorithmic complexity	
	Time complexity	Space complexity
AF	$O(n^2k^2)$	$O(n^2)$
MF	$O(n^2k^2 \log k)$	$O(n^2)$
NLM	$O(n^2 \cdot S^2 \cdot P^2)$	$O(n^2)$
BM3D	$O(n^2 \cdot S^2 \cdot P^2)$	$O(n^2)$
DnCNN	$O(L \cdot C \cdot n^2)$	$O(L \cdot C \cdot n^2)$
WNNM	$O(l \cdot n^3)$	$O(n^2)$
GHCTWNNM	$O(l \cdot T \cdot n^2)$	$O(n^2)$

reflects the drawbacks of deep learning, that is, the need for a large amount of sample data for model training. When equipped with a sufficient amount of labeled data, deep learning methods may be a superior solution.

In addition, we conducted a comparative analysis of the computational complexity of different algorithms, and Table 3 presents the time and space complexities. Among them, the time complexity of AF and MF is related to the size of the convolution kernel k. A large value of k can significantly enhance denoising capability, and it will also cause the time complexity to increase exponentially. Similarly, the time complexity of NLM and BM3D algorithms is also affected by the search window S and block size P. The time complexity of DnCNN is affected by the number of network layers L and channels C. By comparing GHCTWNNM and WNNM, we find that GHCTWNNM has significantly lower time complexity than WNNM, especially for large images. The truncation in GHCTWNNM greatly reduces the computational load of SVD. Thus, GHCTWNNM is more efficient for large-scale image data processing. Regarding space complexity, DnCNN's memory-intensive nature primarily stems from its backpropagation mechanism during training, which requires storing a large number of weight parameters across multiple convolutional layers.

Since the results of LIBS experiments are easily affected by environmental factors, we further analyzed the anti-noise performance of different algorithms. Taking sample no. 1 as an example, we normalized the LIBS spectrum and then added extra Gaussian noise to the measured LIBS spectrum, and the noise levels can be reflected by the value of σ^2. According to the results in Fig. 10, we observed that the GHCTWNNM algorithm shows obvious advantages in all levels of noise. When $\sigma^2 = 0$, the GHCTWNNM algorithm shows an improvement of nearly 4 dB over the second-best SOMA algorithm. In addition, as the added noise increases, the ΔSNR of all algorithms decreases. Despite this, the GHCTWNNM algorithm has demonstrated the best performance when σ^2 ranges from 0 to 1. It particularly maintains a high value of ΔSNR in high-noise environments. Table S3† gives the SNR value of characteristic spectral lines at Al396.15 nm after adding noise with different variances. When the variance of the added noise is 0.8 and 1, the SNR value is lower than 10 dB. Under severe noise conditions with additive noise variances of 1 (SNR < 10 dB), our proposed GHCTWNNM algorithm achieves a nearly 5 dB enhancement in ΔSNR, indicating its excellent robustness and noise adaptability. However, the traditional approaches (*e.g.*, average/median filtering) perform poorly under high-noise conditions due to excessive smoothing or edge loss.

3.2.3 Quantitative analysis of the denoised LIBS spectrum. In this Section, we focused on the quantitative analysis of the Mn and Al elements in LIBS spectra. By comparing the quantitative analysis accuracy, the effectiveness of different denoising algorithms can be assessed. Therefore, this also involves converting the denoised 2D LIBS images back into the 1D LIBS spectrum. Fig. 11 shows the raw and denoised LIBS spectrum by the GHCTWNNM algorithm of sample no. 1. Taking the localized magnification of the LIBS spectrum figure in the 820–900 nm band as an example, the raw LIBS spectrum is significantly disturbed by the continuous background noise, with almost all non-characteristic spectral lines affected by noise. After applying spectrum denoising, the noise in the spectrum is significantly diminished, and the LIBS spectrum continuity is also enhanced. At the same time, the peak values of the characteristic spectral lines exhibit varying degrees of increase or decrease. This fluctuation is attributed to the noise, which may induce random alterations in the peak values of the original characteristic spectral lines.[41]

Then we conducted quantitative analysis of LIBS before and after denoising. For the 40 groups of the steel slag samples shown in Table S1,† we randomly divided them into the train set

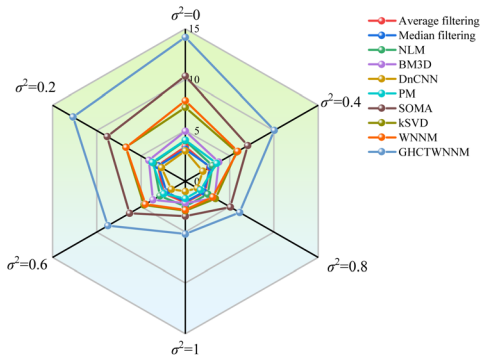

Fig. 10 The radar chart of denoising algorithm performance under different noise conditions.

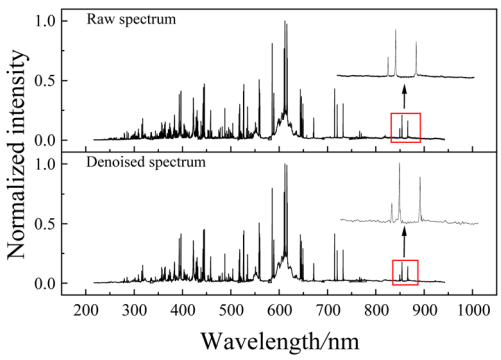

Fig. 11 The normalized intensity of the raw and denoised LIBS spectrum of sample no. 1.

Table 4 The R^2 results of the quantitative analysis before and after LIBS spectrum denoising. c and γ are the penalty factor and the radial basis kernel function of the SVR algorithm

Denoising algorithm		Mn				Al			
		Train	Test	c	γ	Train	Test	c	γ
Without denoising		0.8484	0.8616	75.96	0.156	0.7079	0.7271	2.42	0.120
WT	Sqtwolog	0.8651	0.8732	85.25	0.151	0.7474	0.7858	99.65	0.001
	MiniMaxi	0.8754	0.8833	75.23	0.001	0.7510	0.7823	74.26	0.001
	Heursure	0.9042	0.9134	87.55	0.347	0.8190	0.8499	37.23	0.412
	Birge Massart	0.9285	0.9342	100	0.001	0.8629	0.8922	16.59	0.741
GHCTWNNM		**0.9642**	**0.9899**	77.99	0.001	**0.9641**	**0.9831**	44.49	0.280

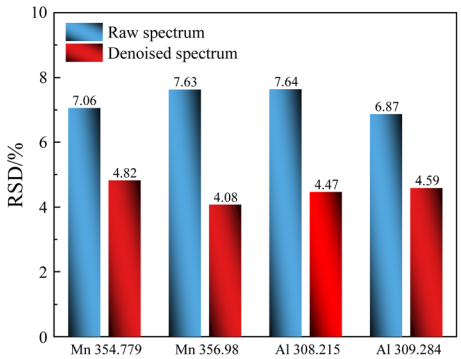

Fig. 12 The RSD results of the raw and denoised spectrum.

and the test set in a ratio of 3 : 1, and the samples of the test set are marked with #. Table 4 presents the quantitative results for the Mn and Al elements before and after denoising. Here, we employ the PSO-SVR algorithm for multivariate quantitative analysis, and the penalty factor c and the radial basis kernel function γ are also displayed. Additionally, we select the WT denoising algorithm with four different wavelet thresholding strategies for comparison. The detail information of these four strategies can be found in the ESI.† According to the results in Table 4, we can conclude that the multivariate quantitative analysis results have been significantly improved after spectrum denoising by the GHCTWNNM algorithm. The R^2 for the concentration prediction results for Mn and Al elements increased by approximately 0.12 and 0.26 on both the train and test set, respectively. Compared to the WT method, the GHCTWNNM algorithm has achieved an obvious increase in R^2. This confirms that our proposed GHCTWNNM algorithm not only performs well in LIBS image denoising but also effectively enhances the quantitative analysis accuracy.

Finally, we compared the stability of the LIBS before and after denoising. We selected the four characteristic spectral lines: Mn 354.779 nm, Mn 356.98 nm, Al 308.215 nm, and Al 309.284 nm. The RSD results of these lines are shown in Fig. 12. Overall, the RSD values of the denoised spectrum are all lower than those of the raw spectrum, and the reduction is about 2–3%. Taking the spectral line at Mn 356.98 nm as an example, after spectrum denoising, the RSD is reduced from 7.63% to 4.08%. These results fully demonstrate that our proposed GHCTWNNM algorithm can not only reduce spectrum noise but also effectively enhance the stability and reliability.

4. Conclusion

In this paper, we introduced a LIBS spectra denoising method based on the GHCTWNNM algorithm. In view of the numerous mature achievements already made in the field of image denoising, we attempt to convert the LIBS signal denoising task into an image-based denoising task, aiming to utilize the advantages of image denoising to enhance the denoising performance of LIBS spectra. To better assess the denoising performance, we conducted the analysis from the perspectives of SNR of elemental characteristic spectral lines, quantitative analysis accuracy, and spectra stability. The results show that the GHCTWNNM algorithm outperforms nine other image denoising algorithms, indicating superior noise reduction capabilities. And it shows a greater adaptability to various noise conditions. In addition, the Al element quantitative analysis results of the LIBS spectra show a notable enhancement, where the R^2 value increases by about 0.26 after the application of the GHCTWNNM algorithm. Compared with the WT method, the R^2 also has a significant improvement. Finally, we also found that after denoising, not only is the SNR of the spectra improved, but also the stability of the spectra is enhanced. The above experimental results indicate that the LIBS denoising method based on the GHCTWNNM algorithm can effectively improve the SNR of the spectra, and enhance the quantitative analysis accuracy. By employing this approach, we can significantly mitigate the quantitative analysis errors induced by noise, thereby robustly enhancing the precision and dependability of LIBS. This, in turn, establishes a firm foundation for its extensive application and further expansion across a multitude of related domains.

Data availability

The relevant experimental data are available on request.

Author contributions

Shengjie Ma: investigation, conceptualization, software, formal analysis, visualization, writing the original draft. Shilong Xu:

methodology, writing – review and editing. Congyuan Pan: software, resources. Jiajie Fang: investigation, visualization. Fei Han: investigation. Xi Wang: data curation. Yuhao Xia: visualization. Wanying Ding: visualization. Yihua Hu: writing – review and editing, supervision, conceptualization.

Conflicts of interest

There are no conflicts to declare.

Acknowledgements

This work was supported by the Hefei Comprehensive National Science Center (KY23C502), the Postgraduate Scientific Research Innovation Project of Hunan Province (CX20230024), the Scientific Research Project of National University of Defense Technology (22-ZZCX-07), Anhui Provincial Natural Science Foundation (2208085QF219), and the Youth Independent Innovation Science Foundation Project of National University of Defense Technology (ZK23-45). Thanks to Hefei GStar Intelligent Control Technical Co. Ltd. for the LIBS spectrum data.

Notes and references

1 Z. Wang, M. S. Afgan, W. L. Gu, *et al.*, Recent advances in laser-induced breakdown spectroscopy quantification: From fundamental understanding to data processing, *Trac. Trends Anal. Chem.*, 2021, **143**, 116385.

2 V. Gardette, V. Motto-Ros, C. Alvarez-Llamas, *et al.*, Laser-induced breakdown spectroscopy imaging for material and biomedical applications: recent advances and future perspectives, *Anal. Chem.*, 2023, **95**(1), 49–69.

3 R. S. Harmon and G. S. Senesi, Laser-induced breakdown spectroscopy–a geochemical tool for the 21st century, *Appl. Geochem.*, 2021, **128**, 104929.

4 A. K. Myakalwar, C. Sandoval, M. Velásquez, *et al.*, LIBS as a spectral sensor for monitoring metallic molten phase in metallurgical applications—a review, *Minerals*, 2021, **11**(10), 1073.

5 Y. Zhao, Z. Li, S. Li, *et al.*, A review of in-situ high-temperature characterizations for understanding the processes in metallurgical engineering, *Int. J. Miner. Metall. Mater.*, 2024, **31**(11), 2327–2344.

6 J. D. Pedarnig, S. Trautner, S. Grünberger, *et al.*, Review of element analysis of industrial materials by in-line laser-induced breakdown spectroscopy (LIBS), *Appl. Sci.*, 2021, **11**(19), 9274.

7 Y. Zhang, T. Zhang and H. Li, Application of laser-induced breakdown spectroscopy (LIBS) in environmental monitoring, *Spectrochim. Acta Part B At. Spectrosc.*, 2021, **181**, 106218.

8 D. A. Gonçalves, G. S. Senesi and G. Nicolodelli, Laser-induced breakdown spectroscopy applied to environmental systems and their potential contaminants. An overview of advances achieved in the last few years, *Trends Environ. Anal. Chem.*, 2021, **30**, e00121.

9 T. Chen, T. Zhang and H. Li, Applications of laser-induced breakdown spectroscopy (LIBS) combined with machine learning in geochemical and environmental resources exploration, *Trac. Trends Anal. Chem.*, 2020, **133**, 116113.

10 R. S. Harmon and G. S. Senesi, Laser-induced breakdown spectroscopy-a geochemical tool for the 21st century, *Appl. Geochem.*, 2021, **128**, 104929.

11 O. A. Al-Najjar, Y. S. Wudil, U. F. Ahmad, *et al.*, Applications of laser-induced breakdown spectroscopy in geotechnical engineering: a critical review of recent developments, perspectives and challenges, *Appl. Spectrosc. Rev.*, 2023, **58**(10), 687–723.

12 R. Zhang, S. Hu, C. Ma, *et al.*, Laser-induced breakdown spectroscopy (LIBS) in biomedical analysis, *Trac. Trends Anal. Chem.*, 2024, 117992.

13 A. V. Skalny, T. V. Korobeinikova, M. Aschner, *et al.*, Medical application of laser-induced breakdown spectroscopy (LIBS) for assessment of trace element and mineral in biosamples: Laboratory and clinical validity of the method, *J. Trace Elem. Med. Biol.*, 2023, **79**, 127241.

14 E. Tognoni and G. Cristoforetti, Signal and noise in laser-induced breakdown spectroscopy: an introductory review, *Opt Laser. Technol.*, 2016, **79**, 164–172.

15 P. A. Benedetti, G. Cristoforetti, S. Legnaioli, *et al.*, Effect of laser pulse energies in laser-induced breakdown spectroscopy in double-pulse configuration, *Spectrochim. Acta Part B At. Spectrosc.*, 2005, **60**(11), 1392–1401.

16 V. I. Babushok, Jr F. C. DeLucia, J. L. Gottfried, *et al.*, Double pulse laser ablation and plasma: Laser-induced breakdown spectroscopy signal enhancement, *Spectrochim. Acta Part B At. Spectrosc.*, 2006, **61**(9), 999–1014.

17 T. R. Loree and L. J. Radziemski, Laser-induced breakdown spectroscopy: time-integrated applications, *Plasma Chem. Plasma Process.*, 1981, **1**, 271–279.

18 S. Fang, S. Wu, Z. Chen, *et al.*, Recent progress and applications of Raman spectrum denoising algorithms in chemical and biological analyses: A review, *Trac. Trends Anal. Chem.*, 2024, 117578.

19 J. G. R. Leandro, F. B. Gonzaga and J. V. F. Latorraca, Discrimination of wood species using laser-induced breakdown spectroscopy and near-infrared reflectance spectroscopy, *Wood Sci. Technol.*, 2019, **53**(5), 1079–1091.

20 S. Xie, T. Xu, X. Han, *et al.*, Accuracy improvement of quantitative LIBS analysis using wavelet threshold de-noising, *J. Anal. At. Spectrom.*, 2017, **32**(3), 629–637.

21 P. Lu, Z. Zhuo, W. Zhang, *et al.*, Accuracy improvement of quantitative LIBS analysis of coal properties using a hybrid model based on a wavelet threshold de-noising and feature selection method, *Appl. Opt.*, 2020, **59**(22), 6443–6451.

22 B. Xu, Z. Lin, Z. Xu, *et al.*, Denoising preprocessing using novel wavelet threshold functions in laser-induced breakdown spectroscopy based on fiber laser, *J. Anal. At. Spectrom.*, 2023, **38**(5), 1032–1042.

23 X. He, C. Wang, R. Zheng, *et al.*, GPR image denoising with NSST-UNET and an improved BM3D, *Digit. Signal Process.*, 2022, **123**, 103402.

24 K. Chen, X. Pu, Y. Ren, *et al.*, TEMDNet: A novel deep denoising network for transient electromagnetic signal with signal-to-image transformation, *IEEE Trans. Geosci. Rem. Sens.*, 2020, **60**, 1–18.
25 M. Guo, X. Meng, X. Chen, *et al.*, Seismic Noise Suppression Method Based on Wave-Unet and Attention Mechanism, *IEEE Trans. Geosci. Rem. Sens.*, 2024, **62**, 1–12.
26 J. Chen, J. Pisonero, S. Chen, *et al.*, Convolutional neural network as a novel classification approach for laser-induced breakdown spectroscopy applications in lithological recognition, *Spectrochim. Acta Part B At. Spectrosc.*, 2020, **166**, 105801.
27 Y. Cai, Z. Yao, X. Cheng, *et al.*, Deep metric learning framework combined with Gramian angular difference field image generation for Raman spectra classification based on a handheld Raman spectrometer, *Spectrochim. Acta Mol. Biomol. Spectrosc.*, 2023, **303**, 123085.
28 S. Gu, L. Zhang, W. Zuo, *et al.*, Weighted nuclear norm minimization with application to image denoising, *Proceedings of the IEEE Conference on Computer Vision and Pattern Recognition*, 2014, pp. 2862–2869.
29 W. Zuo, L. Zhang, C. Song, *et al.*, Texture enhanced image denoising via gradient histogram preservation, *Proceedings of the IEEE Conference on Computer Vision and Pattern Recognition*, 2013, pp. 1203–1210.
30 Z. Liu, X. Chen, J. Hu, *et al.*, An alternating direction method of multipliers for solving user equilibrium problem, *Eur. J. Oper. Res.*, 2023, **310**(3), 1072–1084.
31 L. Song, Z. Ge and E. Y. Lam, Dual alternating direction method of multipliers for inverse imaging, *IEEE Trans. Image Process.*, 2022, **31**, 3295–3308.
32 J. Ma, Z. Cheng, X. Zhang, *et al.*, Alternating direction method of multipliers for constrained iterative LQR in autonomous driving, *IEEE Trans. Intell. Transport. Syst.*, 2022, **23**(12), 23031–23042.
33 L. Fan, X. Li, H. Fan, *et al.*, Adaptive texture-preserving denoising method using gradient histogram and nonlocal self-similarity priors, *IEEE Trans. Circ. Syst. Video Technol.*, 2018, **29**(11), 3222–3235.
34 A. Erler, D. Riebe, T. Beitz, *et al.*, Soil nutrient detection for precision agriculture using handheld laser-induced breakdown spectroscopy (LIBS) and multivariate regression methods (PLSR, Lasso and GPR), *Sensors*, 2020, **20**(2), 418.
35 S. Kashiwakura and K. Wagatsuma, Selection of atomic emission lines on the mutual identification of austenitic stainless steels with a combination of laser-induced breakdown spectroscopy (LIBS) and partial-least-square regression (PLSR), *ISIJ Int.*, 2020, **60**(6), 1245–1253.
36 E. Képeš, J. Vrábel, O. Adamovsky, *et al.*, Interpreting support vector machines applied in laser-induced breakdown spectroscopy, *Anal. Chim. Acta*, 2022, **1192**, 339352.
37 M. Yao, G. Fu, T. Chen, *et al.*, A modified genetic algorithm optimized SVM for rapid classification of tea leaves using laser-induced breakdown spectroscopy, *J. Anal. At. Spectrom.*, 2021, **36**(2), 361–367.
38 F. Zhang, X. Tang, A. Tong, *et al.*, Baseline correction for infrared spectra using adaptive smoothness parameter penalized least squares method, *Spectrosc. Lett.*, 2020, **53**(3), 222–233.
39 L. Lin, H. He, R. Xue, *et al.*, Direct and quantitative assessments of near-infrared light attenuation and spectroscopic detection depth in biological tissues using surface-enhanced Raman scattering, *Med-X*, 2023, **1**(1), 9.
40 K. Zhang, W. Zuo, Y. Chen, *et al.*, Beyond a gaussian denoiser: Residual learning of deep CNN for image denoising, *IEEE Trans. Image Process.*, 2017, **26**(7), 3142–3155.
41 H. W. Duan, S. S. Ma, L. J. Han, *et al.*, A novel denoising method for laser-induced breakdown spectroscopy: improved wavelet dual threshold function method and its application to quantitative modeling of Cu and Zn in Chinese animal manure composts, *Appl. Opt.*, 2017, **134**, 262–269.